The molecular architecture of lamins in somatic cells

Yagmur Turgay[1], **Matthias Eibauer**[1], **Anne E. Goldman**[2], **Takeshi Shimi**[2], **Maayan Khayat**[3], **Kfir Ben-Harush**[4], **Anna Dubrovsky-Gaupp**[1], **K. Tanuj Sapra**[1], **Robert D. Goldman**[2], and **Ohad Medalia**[1,3,*]

[1]Department of Biochemistry, University of Zurich, Winterthurerstrasse 190, 8057 Zurich, Switzerland [2]Department of Cell and Molecular Biology, Northwestern University Feinberg School of Medicine, 303 E Chicago Avenue, Chicago, IL 60611, USA [3]Department of Life Sciences and the National Institute for Biotechnology in the Negev, Ben-Gurion University, 84105 Beer-Sheva, Israel [4]Department of Chemical Engineering, Shamoon College of Engineering, Jabotinsky 84, 77245 Ashdod, Israel

Abstract

The nuclear lamina is a fundamental constituent of metazoan nuclei. It is composed mainly of lamins, which are intermediate filament proteins that assemble into a filamentous meshwork, bridging the nuclear envelope and chromatin [1–4]. Besides providing structural stability to the nucleus [5,6], the lamina is involved in many nuclear activities, including chromatin organization, transcription and replication [7–10]. However, the structural organization of the nuclear lamina is poorly understood. Here, we use cryo-electron tomography (cryo-ET) to obtain a detailed view of the organization of the lamin meshwork within the lamina. Data analysis of individual lamin filaments resolves a globular-decorated fiber appearance and shows that A- and B-type lamins assemble into tetrameric 3.5 nm thick filaments. Thus, lamins exhibit a structure that is remarkably different from the other canonical cytoskeletal elements. Our findings define the architecture of the nuclear lamin meshworks at molecular resolution, providing insights into their role in scaffolding the nuclear lamina.

A first glimpse into the structure of the lamin meshwork was accomplished with transmission electron microscopy by visualizing isolated NEs from *Xenopus laevis* oocytes [11]. A 3D structured illumination microscopy (3D-SIM) study revealed spatial segregation of lamin isoforms defining separate meshworks in nuclei of mammalian somatic cells [12]. Visualization of nuclei in intact multicellular and unicellular eukaryotes, by cryo-ET, showed short filaments at the nuclear periphery [13,14]. However, neither the detailed structure nor the identity of these filaments has been resolved. This is attributable to the crowded environment within the lamina and its surroundings, including lamin binding

*Corresponding author: omedalia@bioc.uzh.ch, phone: +41 (0) 44 635 5522, fax: +41 44 635 6805.

proteins, the abundance of heterochromatin at the nucleoplasmic face of the lamina and also a complex cage of cytoplasmic IFs, in mammalian somatic cells [15]. The components surrounding the lamina are typically resistant to the moderate chemical extraction procedures required to preserve the native structures. A careful handling and sample preparation approach is therefore needed to facilitate proper structural analysis of the nuclear lamina.

To obtain an unobstructed view of the lamin meshwork, we utilized vimentin-null mouse embryonic fibroblasts (MEFs), which do not contain cytoplasmic IFs and display indistinguishable organization of lamins and expression levels as compared to wildtype MEFs (Extended Data Fig. 1a and b). For cryo-ET imaging, cells were cultivated on EM-grids prior to the removal of the plasma membrane and cytoplasmic content by a short exposure to a mild detergent (Extended Data Fig. 1c and d). Subsequently, nuclei were treated with nuclease to remove most of the chromatin, followed by rapid vitrification (Extended Data Fig. 1e). This procedure retains the nuclear lamins and lamina associated proteins at the nuclear periphery (Extended Data Fig. 1c and d).

Due to their large size (~10–20 μm in diameter) nuclei can be easily identified at low magnification in cryo-EM images, confirming successful sample preparation and preservation of the overall size and shape of nuclei (Extended Data Fig. 2a–c). The reconstructed cryo-tomograms reveal the presence of ~3.5 nm thick filaments forming a complex meshwork at the nuclear periphery, underneath nuclear pore complexes (NPCs) (Fig. 1a and b). These filaments vary in length and display a pattern of sparsely and densely packed regions (Fig. 1a), which are also detected above dense nuclear material (presumably chromatin remnants, Extended Data Fig. 2c–e). Statistical analysis of these filaments indicated a length of 380 ± 122 nm (Fig. 1c). The persistence length distribution of these filaments varied between 50 nm – 2700 nm (Fig. 1d), indicating a high degree of flexibility, which is in agreement with measurements of the previously analysed *C. elegans* lamin [16] and the short filaments found at the nuclear periphery in HeLa cells [14]. Furthermore, we show that these filaments are packaged into a 14 ± 2 nm thick layer (Fig. 1e).

For a more complete analysis of lamin filaments organization, we extracted 25 sub-regions containing filaments from the tomograms of nine nuclei (Fig. 2a), and evaluated the properties of their meshworks. Visual inspection indicates that there is a large variability in the number of spaces, i.e. regions containing few if any filaments within the mesh. There is also significant variability in the number of filaments surrounding these spaces and the distance between adjacent filaments. The spaces represent regions containing proteins and chromatin, which are likely removed during sample preparation. The area occupied by filaments is 50 ± 10 % of the total nuclear surface (Fig. 2b), indicating a generally dense meshwork underlining the INM. Thus, the filaments occupy about 12.5% of the entire volume of the ~14 nm thick lamina. The high occupancy of filaments at the nuclear periphery is in accordance with their proposed roles in regulating the mechanical properties of the nucleus and in providing a scaffold for tethering peripheral elements of heterochromatin to the lamina.

To prove that these filaments are composed of A- and B-type lamins, cells were prepared as described above, followed by labeling with either lamin A/C or lamin B1 antibodies decorated with 6 nm gold-labeled protein A and imaging by cryo-ET. Surface rendered views of labeled lamin A/C and lamin B1 show decoration of filaments with the gold-conjugates, while control nuclei (not treated with primary antibody) are not labeled (Fig. 2c and Extended Data Fig. 3), confirming that both A- and B-type lamins are major constituents of the filaments observed.

Next, we determined if A- and B type lamins differ with respect to their localization within sparse or dense regions of the filamentous meshwork. We analyzed the position and density of gold-labeled A- and B-type lamin filaments in nine sub-tomograms each (Extended Data Fig. 3c and d). Statistical analysis of the distribution of the gold labels demonstrates that both lamin sub-types are present throughout the meshwork and are found in both densely packed and sparsely occupied sub-regions within the lamina. This reflects the similarity of A- and B-type lamin-filament structural assemblies.

To study the relative spatial distributions and densities of the different lamin types within the nuclear lamina (Fig. 2d and Extended Data Fig. 4) we co-immunogold-labeled A- and B-type lamins with different sized colloidal gold conjugates (6 nm and 10 nm, respectively). Thirty-six volumes containing lamin meshwork structures were acquired and analyzed by cryo-ET. An assembly of these data into a collage, shows the coordinates of the 6 nm and 10 nm lamin A/C and lamin B1 gold labels as green and red circular Gaussian functions, with a full width at half maximum (FWHM) of 10 nm (Fig. 2e, left image). To correlate these data with previously published 3D-SIM analyses (at 110–130 nm resolution), we filtered the labeled gold colloids to a FWHM of 120 nm (Fig. 2e, right). Comparison with the 3D-SIM analysis of untreated wildtype MEFs (Fig. 2f, adopted from [12]) shows remarkable similarities, confirming the segregation of the different lamin isoforms within the lamina meshwork.

The short persistence length of lamin filaments (Fig. 1d) suggests that they are highly flexible, making it difficult to reconstruct their structure in 3D. However, to unravel the structural features that are responsible for the mechanical properties of the lamins, it is important to determine the molecular architecture of single filaments in their native environment. Therefore, sub-tomograms containing single filaments were extracted from cryo-tomograms of NE regions and subjected to averaging and 2D classification procedures (see Methods and Extended Data Fig. 5a and b). The class averages provide insight into the supramolecular organization of lamin filaments *in situ* and reveal globular structures along the filaments (Fig. 3a, b and c), which may represent lamin Ig-fold domains ([17], Extended Data Fig. 5c) or lamin binding partners.

Lamin monomers are composed of a central α-helical coiled-coil rod domain, ~50 nm in length [18], flanked by a non-α-helical N-terminal head and a C-terminal tail domain [19]. The head domain is short (~ 30 aa) [20], while the tail domain is 185–277 residues long and includes a globular Ig-fold, ~3.5 nm in diameter [21]. In solution, lamins form parallel and in register dimers exhibiting two Ig-fold domains located within the C-terminal end of the rod. The dimers further assemble into head-to-tail polymers, arranged in a partially staggered

conformation, in which Ig-domains are found distributed at ~40 nm intervals along the polymer (Extended Data Fig. 5c), causing the characteristic beaded appearance of lamin assemblies [17,22].

Based on the class averages obtained from our data, the thickness of the rod and the globular domains is ~3.5 nm (Fig. 3d). These latter structures repeat every 20 nm alongside the rod and are similar to the size of the lamin Ig-fold domain [21]. The uniform thickness of the rod domain and the appearance of the purported Ig-fold domains (Fig. 3a–c and Extended Data Fig. 6) indicates that the filaments are composed of at least two head-to-tail polymers (Fig. 3e and Extended Data Fig. 7), as one head-to-tail polymer would not exhibit an isotropic coiled-coil diameter of ~3.5 nm [23] (Fig. 3f, dimer). The resulting lamin filament model (Fig. 3e) was used to replace the filaments in the central region of the lamina shown in Fig. 1a, which exemplifies their molecular organization *in situ* (Fig. 4a).

Based on their genealogy, lamins are considered to be the evolutionary ancestors of all cytoskeletal IFs [24]. However, it is apparent that lamins form a different filamentous structure compared to cytoplasmic IF proteins. Figure 4b shows the major cytoskeletal elements for comparison with the nuclear lamins. Microtubules exhibit a 24 nm thick tubular structure [25], filamentous actin assembles into an 8 nm thick helical structure [26], and cytoplasmic IFs, e.g. vimentin, into 10 nm thick filaments. Here, we show that the lamin meshwork is composed of ~3.5 nm thick filaments, which distinguishes them from the other cytoskeletal constituents in higher eukaryotes.

In summary, our study provides a detailed view of the structure of nuclear lamins in mammalian nuclei. We reveal the organization and assemblies of individual lamin filaments at molecular resolution, while avoiding excessive pre-purification approaches.

Mutations in the *LMNA* gene cause a wide range of diseases, collectively called laminopathies. These diseases include muscular dystrophies, lipodystrophies, neuropathies and premature aging [27–29]. In the future, cryo-ET analyses should provide important insights into the structural differences between the lamin meshworks comprising the lamina of normal nuclei and those from patients bearing specific laminopathic mutations. This approach should help to establish disease models at the molecular level, which may pave the way for new therapeutic interventions.

Methods

Cell lines and cell culture

Mouse embryonic fibroblasts null for vimentin (Vimentin$^{-/-}$; [31]) were maintained in DMEM (Sigma-Aldrich, #D5671) containing 10% FCS (Sigma-Aldrich, #F7524), 2 mM L-Glutamine (Sigma-Aldrich, #G7513) and 100 µg/ml penicillin/streptomycin (Sigma-Aldrich, #P0781). Cells were cultivated at 37°C and 5% CO_2 in a humidified incubator. For cryo-ET analysis, cells were cultured on glow-discharged holey carbon EM grids (R2/1, Au 200 mesh; Quantifoil, Jena, Germany).

Antibodies

For immunogold-labeling experiments, rabbit monoclonal antibody directed against the rod domain of mouse lamin A/C (peptide between aa 200–300) (EP4520, ab133256) was purchased from Abcam. Affinity purified and peptide-specific rabbit antibody against the flexible linker region between the rod and the globular domain of human lamin B1 (aa 391–428) [32] was a kind gift of Larry Gerace (Scripps, La Jolla, CA).

Cryo-ET sample preparation

For cryo-ET analysis, Vimentin$^{-/-}$ MEFs were grown to ~80% confluency on EM-grids coated with a carbon mesh (R2/1, Au 200 mesh; Quantifoil, Jena, Germany). Using fine tweezers, EM grids with a homogenous distribution of cells were picked and washed in PBS/2 mM $MgCl_2$ for 5 sec. These grids were then incubated in pre-permeabilization buffer (PBS containing 0.1% Triton-X 100, 10 mM $MgCl_2$, 600 mM KCl and protease inhibitors) for 20–40 sec and subsequently rinsed in PBS/2 mM $MgCl_2$ for 10 sec. Next, the EM-grids were subjected to nuclease treatment using Benzonase (2.5 units/μl in PBS/2 mM $MgCl_2$; Millipore, Benzonase$^®$ Nuclease HC, Purity > 99%) for 30 min at RT. The EM-grids were washed in PBS/2 mM $MgCl_2$ prior to addition of 3 μl of 10 nm or 15 nm fiducial gold marker (Aurion), diluted 1:500 from the original stock. Lastly, the EM-grids were manually blotted for ~3 sec from the reverse side and plunge frozen in liquid ethane.

Immunogold-labeling

For immunogold-labeling of lamins in Vim$^{-/-}$ MEFs, cells were grown to ~80% confluency on gold EM-grids coated with a carbon mesh (R2/1, 200 mesh; Quantifoil, Jena, Germany). After pre-permeabilization and benzonase treatment as described in the Cryo-ET sample preparation section, nuclei on EM-grids were fixed in 4% PFA for 5 min at RT. The EM-grids were quenched in 0.05 M Glycine/PBS for 15 min at RT to inactivate aldehyde groups present after aldehyde fixation. Next, samples were blocked in blocking solution (5% BSA/0.1% cold water fish skin gelatin/PBS; Aurion) for 30 min at RT and subsequently washed 3 × 5 min with the incubation solution (0.2% BSA-c/PBS; Aurion). Immunogold analysis was performed using anti-lamin A/C and anti-lamin B1 (see above) at a dilution of 1:200 in the incubation solution (0.2% BSA-c/PBS; Aurion) for 1h at RT. Next, the EM-grids were washed 6 × 5 min at RT with incubation solution (0.2% BSA-c/PBS; Aurion) prior to treatment with the gold conjugate (protein A coupled to 6 nm gold; Aurion) in incubation solution (0.2% BSA-c/PBS; Aurion) at a dilution of 1:50 for 2 h at RT. After extensive washing (6 × 5 min at RT) with the incubation solution (0.2% BSA-c/PBS; Aurion) and 3 × 5 min with PBS at RT, the EM-grids were manually blotted for ~3 sec from the reverse side and plunge frozen.

Co-immunogold labeling analysis

Cells were treated consecutively using anti-lamin A/C and anti-lamin B1 at a dilution of 1:100 and as described above. Briefly, after treatment with anti-Lamin A/C antibodies for 1h and Prot A conjugate (6 nm) for 2h, samples were postfixed in 4% PFA for 5 min, again quenched in 0.05 M Glycine/PBS for 15 min to inactivate aldehyde groups present after aldehyde fixation and blocked in blocking solution (5% BSA/0.1% cold water fish skin

gelatin/PBS; Aurion) for 30 min. Next, the sample was washed 3×5 min with the incubation solution (0.2% BSA-c/PBS; Aurion) and subjected to a second round of antibody labeling using anti-lamin B1 antibody and Prot A conjugate (10 nm). After extensive washing (6×5 min) with the incubation solution and 3×5 min with PBS, the EM-grids were manually blotted for ~3 sec from the reverse side and plunge frozen.

Cryo-electron tomography

Data acquisition was performed using an FEI Titan Krios transmission electron microscope equipped with a quantum energy filter and a K2-Summit direct electron detector (Gatan, Pleasanton, USA). The microscope was operated at 300 keV in zero-loss mode. Using Digital Micrograph (Gatan, Pleasanton, USA) image stacks were recorded at each tilt angle in the counting mode with an electron flux of ~10 e$^-$/pixel/sec. The image stacks were acquired at a frame rate of 5 fps with a magnification of 42,000× corresponding to a pixel size of 0.34 nm. Tilt-series covered an angular range of −60° to +60° and were recorded at increments of 2°, at a defocus of −6 μm and a maximum cumulative electron dose of 125 e$^-$/Å^2.

For co-immunogold labeling analysis, image stacks were acquired at a frame rate of 5 fps with a magnification of 26,000× corresponding to a pixel size of 0.55 nm. The tilt-series covered an angular range of −60° to +60° and were recorded at increments of 2°, at a defocus of −9 μm and a maximum cumulative electron dose of 90 e$^-$/Å^2.

Drift correction of the image stacks was performed using the built-in module in Digital Micrograph. Next, the tilt-series were CTF corrected [33] and reconstructed using the TOM Toolbox [34].

Analysis of lamin filaments

Out of 36 tomograms, filaments were identified and 7977 sub-volumes of $64 \times 64 \times 64$ pixels (pixel size 1.36 nm, binning 2) were extracted. The filaments in these sub-volumes were then aligned to a cylindrical template parallel to the y-axis and projected in the z-direction. These projections were then visually inspected with an interactive tool (available upon request) written in MATLAB (Mathworks, Natick, USA). Thereby 3524 strongly bent or discontinuous filaments were excluded, leaving 4453 filaments for further analysis. Next, the filaments in the projections were masked and subjected to 2D classification using Relion [35]. After the first round of classification, classes containing strongly distorted filaments were removed to reduce heterogeneity. We then performed another round of classification with the remaining 3880 filaments (pixel size 0.68, binning 1), separating them into 40 classes (Extended Data Fig. 5b).

Image processing

Slices from tomograms were generated in MATLAB using the TOM Toolbox. Segmentation of filaments, NPCs and putative chromatin was performed with Amira (FEI Visualization Sciences Group). The analysis of the occupancy of lamins in the meshwork was performed on projections in z-direction of segmented sub-volumes (340 nm × 340 nm × 68 nm) by calculating the number of pixels defined by the spaces in the mesh divided by the total

number of pixels within the image using the ImageJ-based DiameterJ plugin [36]. For the analysis of immunogold-labeled sub-volumes, segmented filaments were skeletonized in 3D, projected in the z-direction and superimposed with the segmented gold markers using MATLAB (Extended Data Fig. 3c). The persistence length $1/\lambda$ of lamin filaments was calculated by correlating the contour length L and the end-to-end distance R [37]: $<R^2>=(2/\lambda^2)(\lambda L-1+\exp(-\lambda L))$. The contour length and the end-to-end distance of 204 filaments from 30 tomograms were measured manually in 3D using ImageJ. The average filament length was calculated from the contour lengths of all 204 filaments.

Quantification of the gold label density in the co-immunogold labeling experiments was performed using MATLAB. The different sized gold colloids were manually picked from 2D projections of representative sub-volumes (550 nm × 550 nm × 66 nm).

For the comparison of the co-immunogold labeling experiments with 3D-SIM data on A- and B-type lamins, we extracted 47 sub-volumes (550 nm × 550 nm × 66 nm) from 15 tomograms (2250 nm × 2250 nm × 1125 nm). Thirty-six sub-volumes were projected and assembled in random order into a 3.3 μm × 3.3 μm collage. Next, the xy-coordinates of either lamin A/C (6 nm gold particles) or lamin B1 (10 nm gold particles) labels were extracted and represented as 2D Gaussian functions with a full width at half maximum of 10 nm or 120 nm using MATLAB. Finally, these images were colored in green (lamin A/C) and red (lamin B1), respectively, and superimposed using Fiji, in order to model a SIM image with 10 nm resolution (Fig. 2e, left image) or 120 nm resolution (Fig. 2e, right image).

The lamin filament model was built using UCSF Chimera [38]. For the Ig-domain pdb entry 1ifr [21] was used and the linkers between tail and rod were manually drawn. The rod was modelled by using the web-based software CCBuilder [39], based on coiled-coil parameters derived from pdb entries 4dzm, 3r4a, and 3r3k. The pdb structures were converted to electron density maps and filtered to 4 Å resolution.

The nuclear lamina model was built using Amira. The lamin meshwork was assembled in 3D using a sub-volume (see Fig. 1a, central 680 nm × 680 nm × 100 nm) of a cryo-tomogram comprising the nuclear lamina as a template and the lamin filament model (described above) as building block. The NPC structures are from the *Xenopus laevis* oocyte [40] and the INM and ONM was manually drawn.
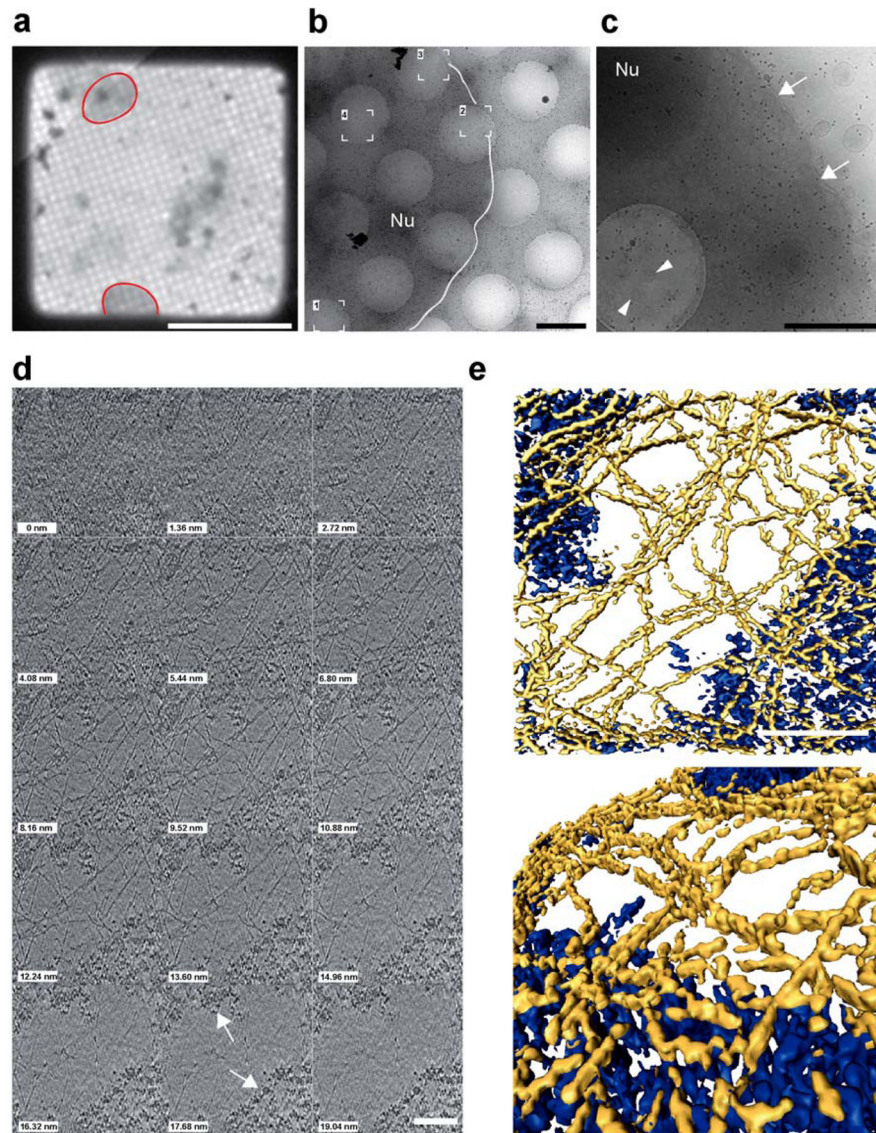
Extended Data
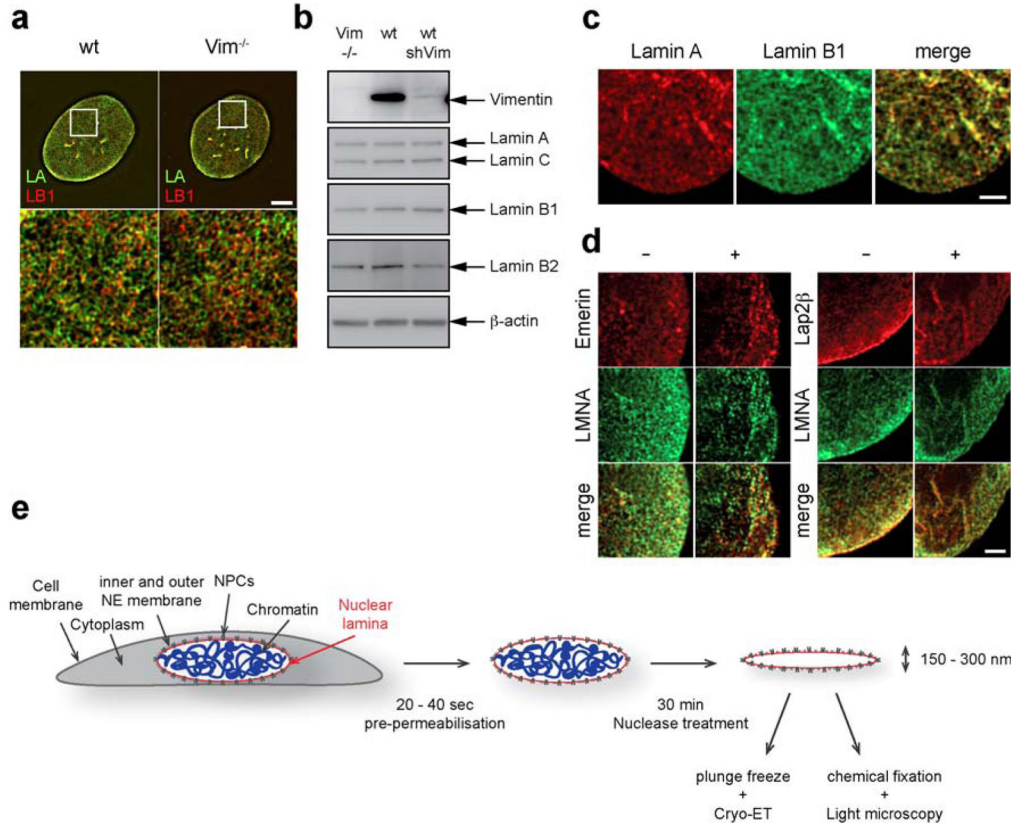
Extended Data Figure 1. Sample preparation of vimentin deficient MEFs for Cryo-ET and 3D-SIM

(a) 3D-SIM images of immunolabeled wt and Vim$^{-/-}$ MEFs shows similar localization and expression of lamin A and lamin B1. Scale bar, 5 μm. (b) Western blot analyses of the indicated MEF cell lines show unchanged expression levels of each of the lamin isoforms and the retention of the lamins following the shRNAi-mediated knockdown of vimentin. (c) 3D-SIM images of pre-permeabilized, nuclease treated and immunolabeled MEFs shows similar localization and expression of lamin A and lamin B1 compared to untreated cells (a). Scale bar, 1 μm. (d) The localization of the lamina associated proteins (LAPs), emerin and Lap2β, exhibit high similarities between pre-permeabilized and nuclease treated (+) and untreated (−) cells, as indicated by 3D-SIM analysis. Scale bar, 1 μm. (e) Illustration of the cryo-ET sample preparation procedure.

**Extended Data Figure 2. vitrified MEF nuclear envelopes on Cryo-ET EM grids**
(a) Low magnification view of two nuclei (encircled by red lines) on a 100×100 μm^2 carbon mesh of an EM-grid. Scale bar, 50 μm. (b) Image shows a part of a nucleus (contoured by the light-grey line). Cryo-tomograms of 1.4×1.4 μm^2 were acquired at various positions within the area indicated (1–4). Representative xy-slices from sub-volumes containing filaments within regions 1–4 are shown in Figure 1b. Scale bar, 2 μm. (c) Higher magnification projection view of a nucleus reveals some of the canonical components of the nucleus, e.g. a region of preserved nuclear double-membrane (white arrows), NPCs (white arrowheads) and a highly dense area with putative chromatin remnants (in the upper left corner). Scale bar, 1 μm. (d) Consecutive 1.36 nm xy-slices show the thickness of the lamin meshwork and displays occasionally observed putative chromatin remnants (white arrows). Scale bar, 100 nm. (e) Rendering shows segmented lamin filaments (yellow) and putative chromatin remnants (blue). This view of the segmented nuclear lamina displays individual

filaments that cross each other at different positions along the z-axis within a boundary of ~14 nm. Scale bar, 100 nm.
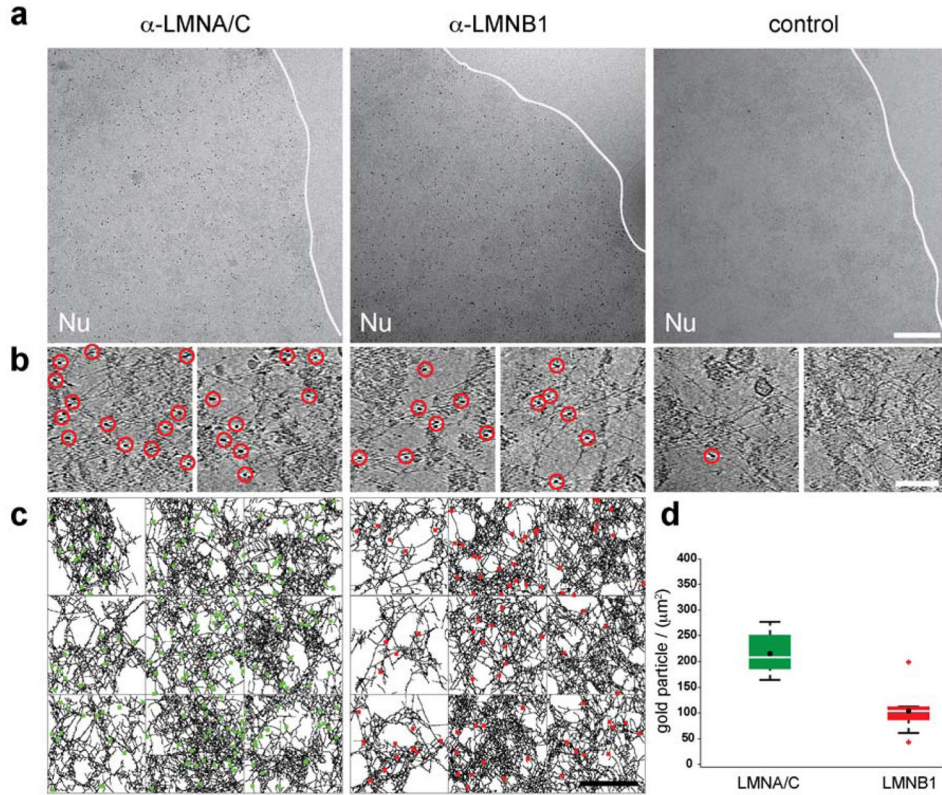
Extended Data Figure 3. Immunogold-labeling of A- and B-type lamins
Nuclei on EM-grids were treated with α-lamin A/C or α-lamin B1 antibodies and labeled with 6 nm gold conjugated protein A prior vitrification and cryo-ET analysis. Control samples were treated with protein A conjugate only. (a) Projection views of nuclei (contoured by the light-grey line) display the distribution of gold conjugate. Scale bar, 200 nm. (b) Zoomed-in images show 9 nm thick xy-slices through reconstructed volumes of the respective immunogold-labeled nuclei. A- and B-type filaments are labeled with gold conjugate as indicated (red circles). Scale bar, 100 nm. (c) Gallery view of immunogold-labeled, segmented and skeletonized filaments from 40 nm thick sub-volumes. Green dots indicate immunogold-labeled lamin A and red dots lamin B1 in nine sub-volumes each, locating both within sparsely and densely packed regions. Scale bar, 200 nm. (d) Box plot shows the immunogold-labeling density of lamin A/C and lamin B1 per μm^2 (+/− SD) from volumes shown in (c) (white line represents the median and black dot the average number of gold particles).
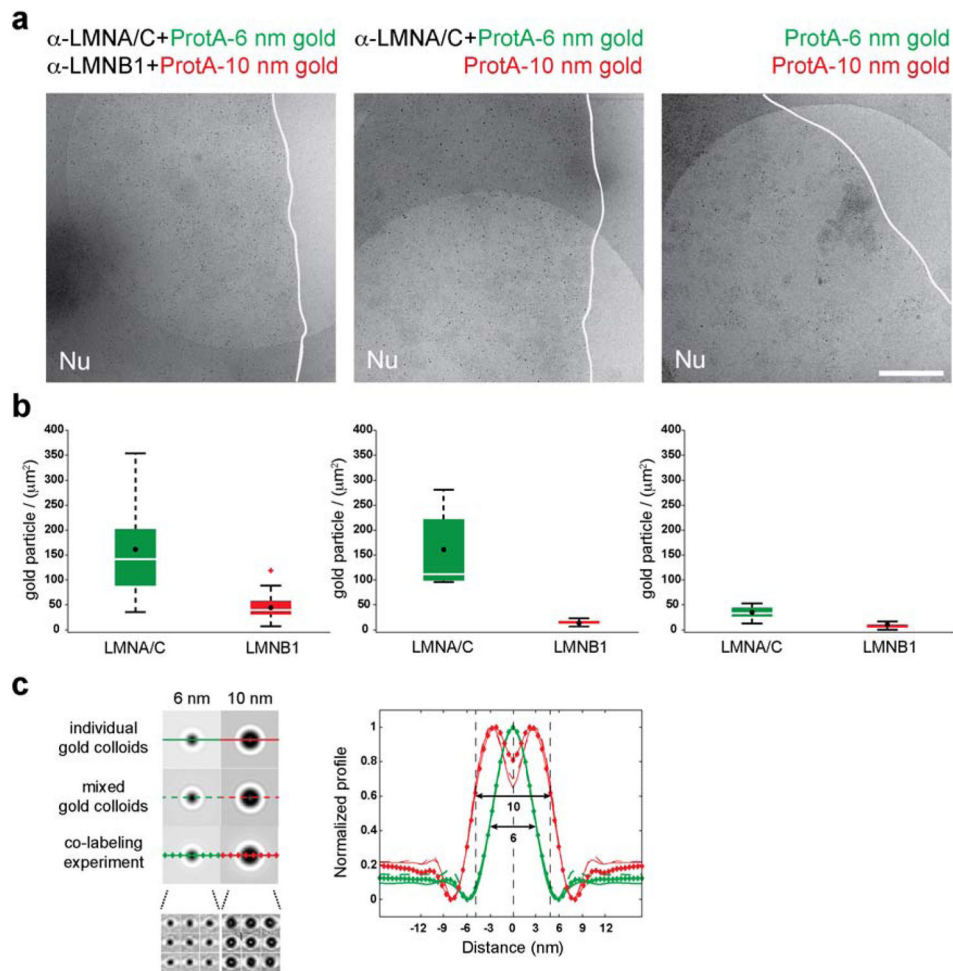
**Extended Data Figure 4. Co-Immunogold-labeling of A- and B-type lamins**

(a) Nuclei on EM-grids were treated with α-lamin A/C and α-lamin B1 and labeled with 6 nm and 10 nm gold conjugates, respectively, prior to vitrification and cryo-ET analysis. Control samples (middle and right) were either treated with α-lamin A/C prior to treatment with 6 nm gold conjugate, post-fixation and subsequent treatment with 10 nm gold conjugate (middle panel), or only with 6 nm and 10 nm gold conjugate (right panel), omitting incubation with antibodies. Large projection views of parts of nuclei (contoured by the light-grey line) display the distribution of gold conjugates under the indicated conditions. Scale bar, 200 nm. (b) Box plots show the labeling density of 6 nm (lamin A/C) and 10 nm (lamin B1) gold particles per μm^2 (+/− SD) under the indicated conditions (white line represents the median and black dot the average amount of gold particles). The number of gold particles was extracted from 47 sub-volumes (left panel), 9 sub-volumes (middle panel) or 11 sub-volumes (right panel). (c) To validate the reliable assignment of small and large gold colloids, 6 nm and 10 nm gold conjugated protein A label were manually picked from samples containing either 6 nm or 10 nm colloids (individual gold colloids), a mixture of both (mixed gold colloids) or from the co-immunogold labeling experiment (lamin A/C and B1 co-labeling experiments) and averaged (n = 200 per condition). The two images at the bottom show a collage of nine individual 6 nm (left) and 10 nm (right) gold conjugated

protein A label, respectively, which were picked from the co-immunogold labeling experiments. The line plot shows the normalized intensity profile of the average diameter of the gold conjugated protein A labels that were picked from the indicated samples. The solid lines show the intensity profile of the averaged gold label from the samples containing only one type of colloid. The dashed lines show the intensity profile of the averaged gold labels picked from a mixture. The lines with diamonds show the profile of the averaged gold labels from the co-immunogold labeling experiment. The line profiles of the 6 nm and 10 nm averaged gold conjugated protein A labels are shown in green and red, respectively. The line plot shows almost identical diameters of the 6 nm or 10 nm gold labels for each condition.
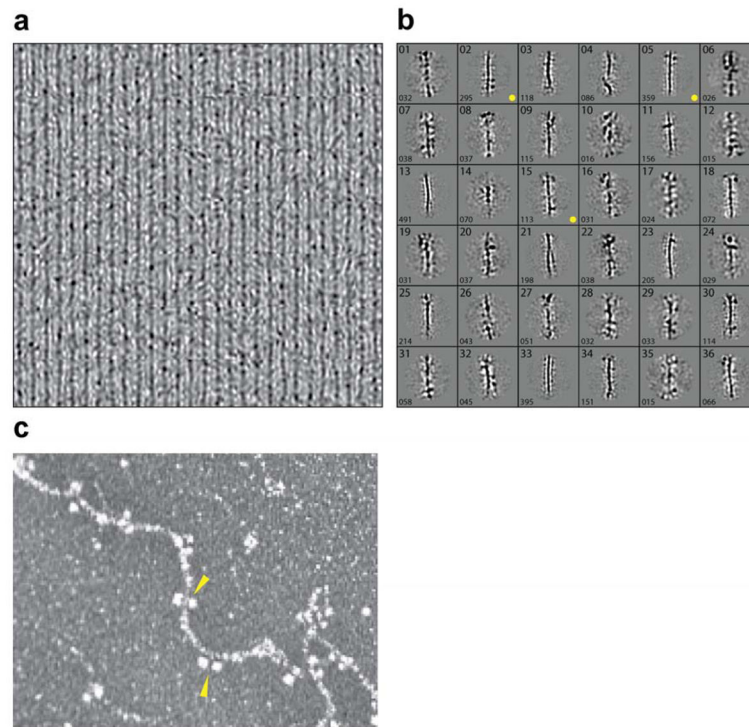
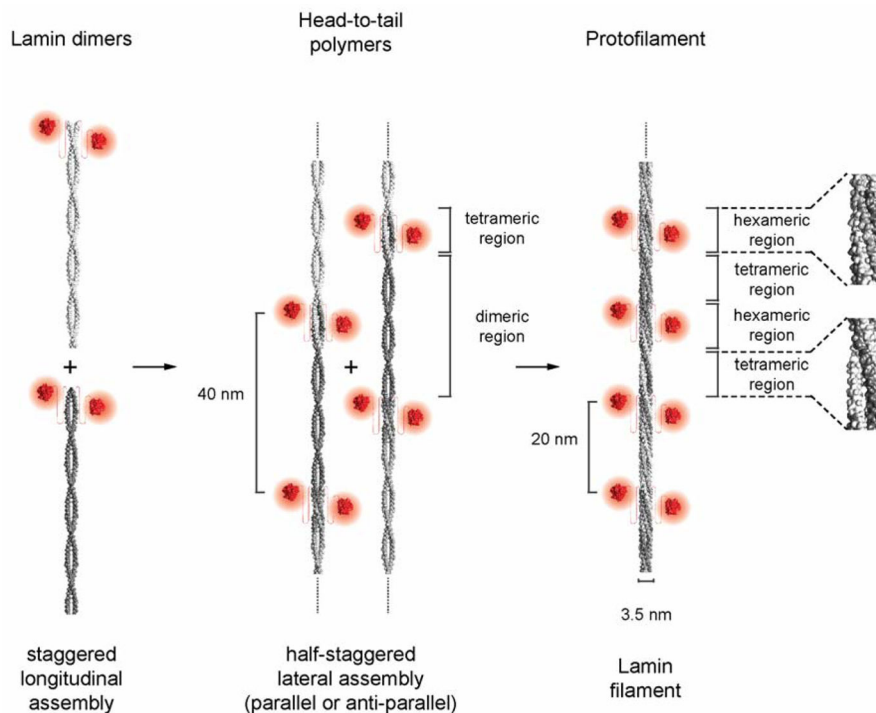**Extended Data Figure 5. Lamin filament classification and averaging**
(a) Gallery view illustrates a set of extracted and aligned filaments used for further analysis. (b) Montage of 36 out of the 40 most populated class averages displays rod-like structures flanked by globular domains at different positions along the central rod. The yellow dots mark four of the most populated classes that are shown in Fig. 3a, b and c. The class index is given in the upper left corner of the sub-frames and the number of particles in the respective class in the lower left corner. (c) Comparison of class averages with index 2 and 5 (Fig. 3c) with *in vitro* data [1] shows remarkable similarities (yellow arrowheads).
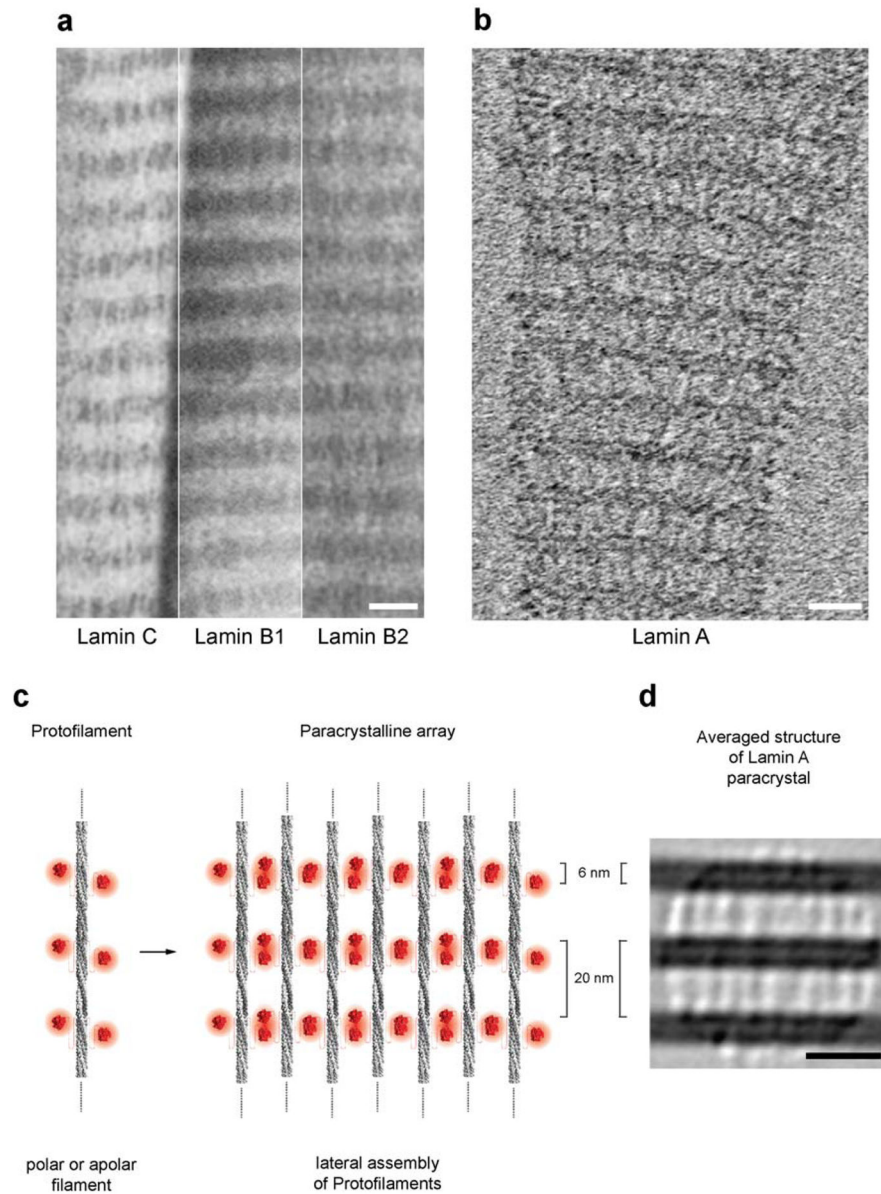
Extended Data Figure 6. Structural analysis of *in vitro* assembled A- and B-type lamin paracrystals

The final step in the *in vitro* assembly of assembled A- and B-type lamins results in the formation of paracrystals that display identical organization, corroborating that A- and B-type lamins assemble into similar structures (a) TEM analysis and comparison of negatively stained human lamin C [2], B1 and B2 paracrystals show an identical striped pattern with 20 nm repeats. Scale bar, 20 nm. (b) Cryo-ET analysis of *in vitro* assembled lamin A shows the same 20 nm repeating pattern compared to the lamin isoforms shown in (a). Scale bar, 20 nm. (c) The model shows the 2D arrangement of lamin protofilaments within a paracrystal. The rod-like structure is shown in grey and the globular tail domains in red. (d) Averaged structure of cryo-tomograms of *in vitro* assembled lamin A as shown in (b) displays the striped pattern comprising the purported Ig-fold domains at distances of 20 nm, comparable

to the spacing of the repeating pairs of globular domains in some structural classes from our *in situ* structural analysis (Fig. 3a and b). The distance of the putative Ig-fold domains within the stripes of the paracrystals is 6 nm. Scale bar, 20 nm.

Extended Data Figure 7. Lamin assembly scheme

Averaging and classification of lamin filaments examined *in situ* show that lamin filaments are composed of two half-staggered head-to-tail polymers. For this, lamin dimers (left) assemble into dimeric head-to-tail polymers exhibiting short overlapping regions, tetrameric in a crosssection (middle). The Ig-domains (red) along the head-to-tail polymer are positioned every ~40 nm. Ultimately, two head-to-tail polymers assemble laterally into a protofilament (right) with a uniformly shaped rod, ~3.5 nm in diameter, containing alternating tetra- and hexameric regions. In this assembly state the Ig-domains are positioned every 20 nm alongside the protofilament.

Acknowledgments

References

1. Aaronson RP, Blobel G. Isolation of nuclear pore complexes in association with a lamina. Proc Natl Acad Sci USA. 1975; 72:1007–1011. [PubMed: 1055359]

2. Burke B, Stewart CL. The nuclear lamins: flexibility in function. Nature reviews Molecular cell biology. 2013; 14:13–24. [PubMed: 23212477]

3. Fawcett DW. On the occurrence of a fibrous lamina on the inner aspect of the nuclear envelope in certain cells of vertebrates. Am J Anat. 1966; 119:129–145. [PubMed: 6007824]

4. Parry DA, Conway JF, Steinert PM. Structural studies on lamin. Similarities and differences between lamin and intermediate-filament proteins. Biochem J. 1986; 238:305–308. [PubMed: 3800939]

5. Dahl KN, Engler AJ, Pajerowski JD, Discher DE. Power-law rheology of isolated nuclei with deformation mapping of nuclear substructures. Biophys J. 2005; 89:2855–2864. [PubMed: 16055543]

6. Lammerding J, et al. Lamin A/C deficiency causes defective nuclear mechanics and mechanotransduction. J Clin Invest. 2004; 113:370–378. [PubMed: 14755334]

7. Camozzi D, et al. Diverse lamin-dependent mechanisms interact to control chromatin dynamics: Focus on laminopathies. Nucleus (Austin, Tex). 2014; 5

8. Dechat T, Gesson K, Foisner R. Lamina-independent lamins in the nuclear interior serve important functions. Cold Spring Harbor symposia on quantitative biology. 2010; 75:533–543. [PubMed: 21209392]

9. Meister P, Mango SE, Gasser SM. Locking the genome: nuclear organization and cell fate. Curr Opin Genet Dev. 2011; 21:167–174. [PubMed: 21345665]

10. Shumaker DK, Kuczmarski ER, Goldman RD. The nucleoskeleton: lamins and actin are major players in essential nuclear functions. Current opinion in cell biology. 2003; 15:358–366. [PubMed: 12787780]

11. Aebi U, Cohn J, Buhle L, Gerace L. The nuclear lamina is a meshwork of intermediate-type filaments. Nature. 1986; 323:560–564. [PubMed: 3762708]

12. Shimi T, et al. Structural organization of nuclear lamins A, C, B1, and B2 revealed by superresolution microscopy. Molecular biology of the cell. 2015; 26:4075–4086. [PubMed: 26310440]

13. Harapin J, et al. Structural analysis of multicellular organisms with cryo-electron tomography. Nat Methods. 2015; 12:634–636. [PubMed: 25961413]

14. Mahamid J, et al. Visualizing the molecular sociology at the HeLa cell nuclear periphery. Science. 2016; 351:969–972. [PubMed: 26917770]

15. Jones JC, Goldman AE, Steinert PM, Yuspa S, Goldman RD. Dynamic aspects of the supramolecular organization of intermediate filament networks in cultured epidermal cells. Cell motility. 1982; 2:197–213. [PubMed: 6756644]

16. Grossman E, et al. Filaments assembly of ectopically expressed Caenorhabditis elegans lamin within Xenopus oocytes. Journal of structural biology. 2012; 177:113–118. [PubMed: 22085746]

17. Stuurman N, Heins S, Aebi U. Nuclear lamins: their structure, assembly, and interactions. Journal of structural biology. 1998; 122:42–66. [PubMed: 9724605]

18. Heitlinger E, et al. Expression of chicken lamin B2 in Escherichia coli: characterization of its structure, assembly, and molecular interactions. The Journal of cell biology. 1991; 113:485–495. [PubMed: 2016332]

19. Herrmann H, Bär H, Kreplak L, Strelkov SV, Aebi U. Intermediate filaments: from cell architecture to nanomechanics. Nature reviews. Molecular cell biology. 2007; 8:562–573. [PubMed: 17551517]

20. Fisher DZ, Chaudhary N, Blobel G. cDNA sequencing of nuclear lamins A and C reveals primary and secondary structural homology to intermediate filament proteins. Proceedings of the National Academy of Sciences of the United States of America. 1986; 83:6450–6454. [PubMed: 3462705]

21. Dhe-Paganon S, Werner ED, Chi YI, Shoelson SE. Structure of the globular tail of nuclear lamin. The Journal of biological chemistry. 2002; 277:17381–17384. [PubMed: 11901143]

22. Ben-Harush K, et al. The supramolecular organization of the C. elegans nuclear lamin filament. Journal of molecular biology. 2009; 386:1392–1402. [PubMed: 19109977]

23. Zaccai NR, et al. A de novo peptide hexamer with a mutable channel. Nature chemical biology. 2011; 7:935–941. DOI: 10.1038/nchembio.692 [PubMed: 22037471]

24. Dittmer TA, Misteli T. The lamin protein family. Genome biology. 2011; 12:222. [PubMed: 21639948]

25. Nogales E, Wolf SG, Khan IA, Luduena RF, Downing KH. Structure of tubulin at 6.5 A and location of the taxol-binding site. Nature. 1995; 375:424–427. DOI: 10.1038/375424a0 [PubMed: 7760939]

26. Galkin VE, Orlova A, Vos MR, Schroder GF, Egelman EH. Near-atomic resolution for one state of F-actin. Structure. 2015; 23:173–182. DOI: 10.1016/j.str.2014.11.006 [PubMed: 25533486]

27. Broers JLV, Ramaekers FCS, Bonne G, Yaou RB, Hutchison CJ. Nuclear lamins: laminopathies and their role in premature ageing. Physiol Rev. 2006; 86:967–1008. [PubMed: 16816143]

28. Worman HJ, Courvalin JC. Nuclear envelope, nuclear lamina, and inherited disease. International review of cytology. 2005; 246:231–279. [PubMed: 16164970]

29. Worman HJ, Ostlund C, Wang Y. Diseases of the nuclear envelope. Cold Spring Harbor perspectives in biology. 2010; 2:a000760. [PubMed: 20182615]

30. Fletcher JM, et al. A basis set of de novo coiled-coil peptide oligomers for rational protein design and synthetic biology. ACS synthetic biology. 2012; 1:240–250. DOI: 10.1021/sb300028q [PubMed: 23651206]

31. Guo M, et al. The role of vimentin intermediate filaments in cortical and cytoplasmic mechanics. Biophys J. 2013; 105:1562–1568. DOI: 10.1016/j.bpj.2013.08.037 [PubMed: 24094397]

32. Schirmer EC, Guan T, Gerace L. Involvement of the lamin rod domain in heterotypic lamin interactions important for nuclear organization. The Journal of cell biology. 2001; 153:479–489. [PubMed: 11331300]

33. Eibauer M, et al. Unraveling the structure of membrane proteins in situ by transfer function corrected cryo-electron tomography. Journal of structural biology. 2012; 180:488–496. DOI: 10.1016/j.jsb.2012.09.008 [PubMed: 23000705]

34. Nickell S, et al. TOM software toolbox: acquisition and analysis for electron tomography. Journal of structural biology. 2005; 149:227–234. DOI: 10.1016/j.jsb.2004.10.006 [PubMed: 15721576]

35. Scheres SH. RELION: implementation of a Bayesian approach to cryo-EM structure determination. Journal of structural biology. 2012; 180:519–530. DOI: 10.1016/j.jsb.2012.09.006 [PubMed: 23000701]

36. Hotaling NA, Bharti K, Kriel H, Simon CG. DiameterJ: A validated open source nanofiber diameter measurement tool. Biomaterials. 2015; 61:327–338. [PubMed: 26043061]

37. Trachtenberg S, Hammel I. Determining the persistence length of biopolymers and rod-like macromolecular assemblies from electron microscope images and deriving some of their …. Microscopy: Science. 2010

38. Pettersen EF, et al. UCSF Chimera--a visualization system for exploratory research and analysis. Journal of computational chemistry. 2004; 25:1605–1612. DOI: 10.1002/jcc.20084 [PubMed: 15264254]

39. Wood CW, et al. CCBuilder: an interactive web-based tool for building, designing and assessing coiled-coil protein assemblies. Bioinformatics. 2014; 30:3029–3035. DOI: 10.1093/ bioinformatics/btu502 [PubMed: 25064570]

40. Eibauer M, et al. Structure and gating of the nuclear pore complex. Nature communications. 2015; 6:7532.
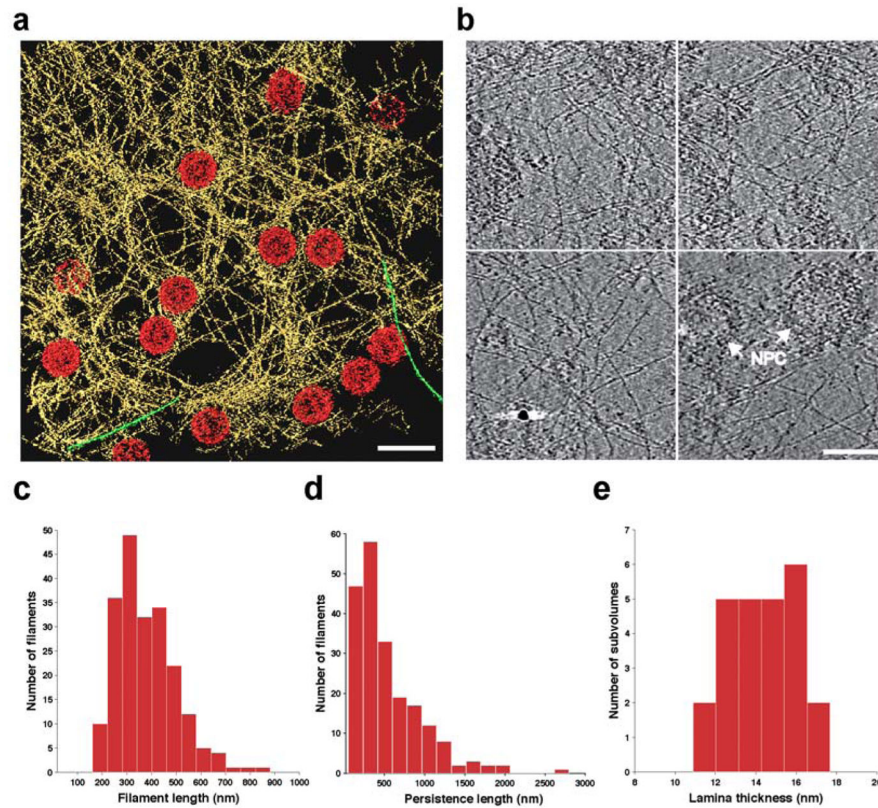
Figure 1. Architecture of the filamentous meshwork of the lamina of the mammalian cell nucleus
(a) Rendered view of a 70 nm thick tomogram slice illustrates the putative lamin filaments (yellow), NPCs (red) and occasionally observed cytoplasmic actin filaments (green) on top of the nucleus. Scale bar, 200 nm. (b) 2 nm thick tomogram slices from different regions of the nuclear lamina (as indicated in Extended Data Fig. 2b). Scale bar, 100 nm. (c) Histogram of the filament length distribution. (d) Histogram of the persistence length distribution (e) Histogram of the thickness of the lamin-containing layer.
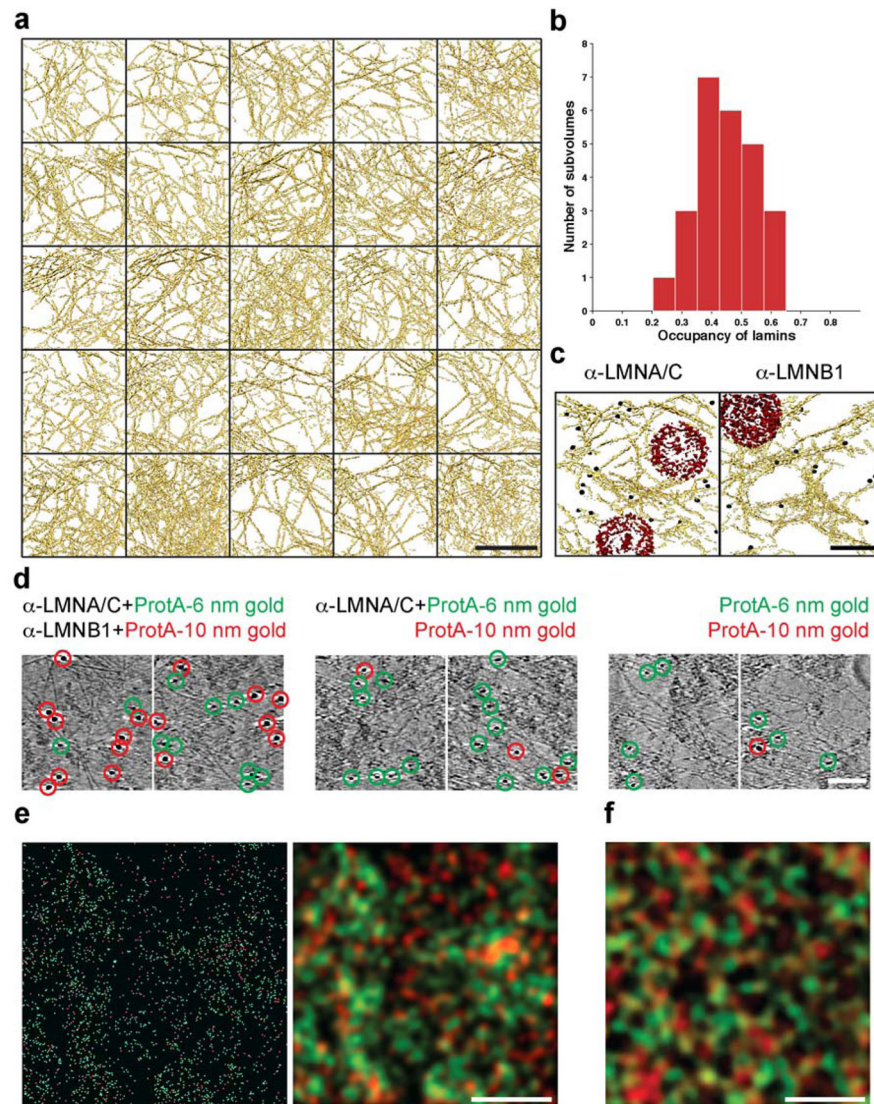
**Figure 2. Characterization of the lamin meshwork**

(a) Rendered lamin filaments from 25 sub-volumes at different positions of nine different nuclei. Scale bar, 200 nm. (b) Histogram of the average occupancy of lamin filaments. (c) Rendered view of 9 nm thick tomogram slices of immunogold-labeled nuclei illustrates lamin filaments (yellow), NPCs (red) and gold conjugates (black). Scale bar, 100 nm. (d) 14 nm thick tomogram slices of co-immunogold-labeled nuclei shows A- and B-type filaments labeled with 6 nm (green circles) and 10 nm (red circles) gold conjugate, respectively. Scale bar, 100 nm. (e) Co-immunogold-labeled A- and B-type lamins from 36 tomographic sub-volumes were combined with lamin A/C in green and lamin B1 in red. The labels were depicted as circular Gaussian functions with a FWHM of 10 nm (e, left) and 120 nm (e, right), respectively. Scale bar is 1 μm. (f) Co-immunofluorescence of lamin A and B1, visualized by 3D-SIM at a resolution of about 110–130 nm [12]. Scale bar, 1 μm.
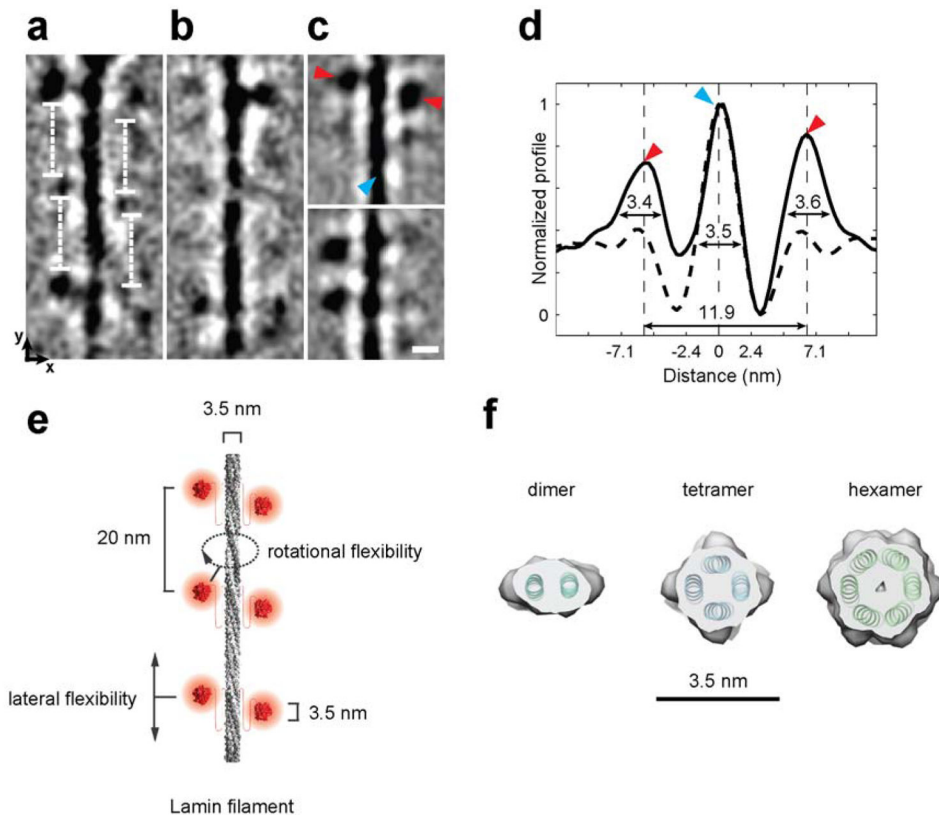
Figure 3. Structural analysis of lamin filaments

(a, b) Some filament classes show alternating distances of ~20 nm between paired globular domains alongside the rod (dashed lines). (c) The globular domains (red arrowheads) appear either on each side of the rod (blue arrowhead) or on the same side of the rod. Scale bar, 5 nm. (d) The dashed line and the continuous line in the normalized intensity profile indicate the average diameter of the rod (blue arrowhead) and the globular domains (red arrowheads) as shown in (c), respectively. The distance between the globular domains on the left and the right side of the rod is ~12 nm. (e) The lamin filament model illustrates the uniform thickness of the rod domain and the positions of the globular domains (red) alongside the rod. (f) A cross-section through a coiled-coil dimer, tetramer and hexamer illustrates the non-isotropic thickness of a dimer, based on the analysis of coiled-coil structures shown in [23,30].

a

b

microtubule	actin	vimentin	lamins

| width: | 24 nm | 8 nm | 10 nm | 3.5 nm |
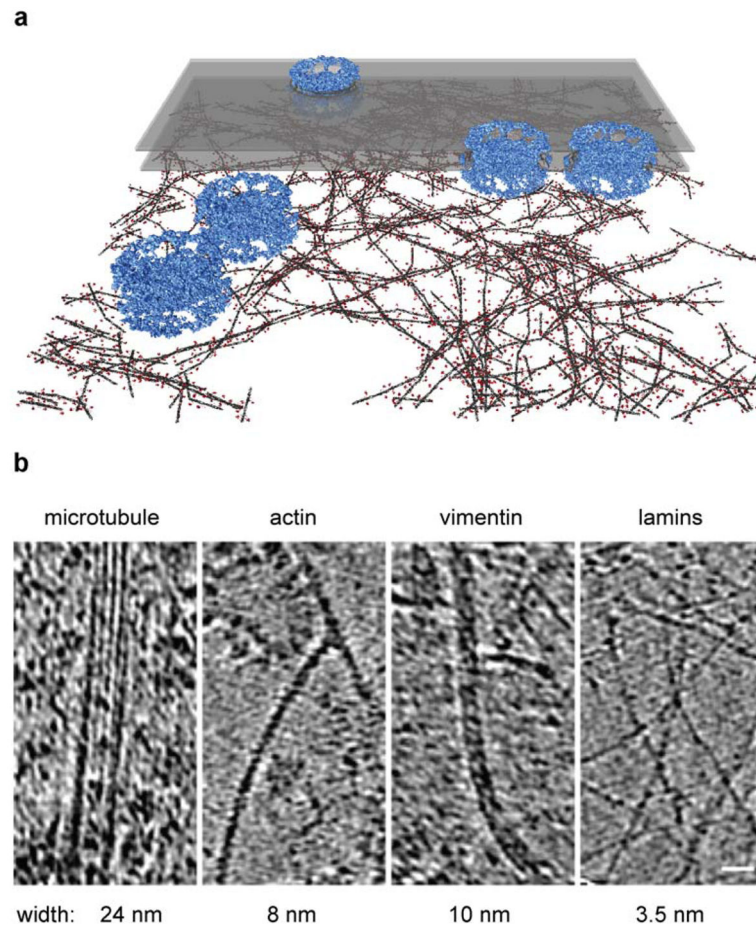
Figure 4. The nuclear lamina and cytoskeletal constituents of mammalian somatic cells
(a) Lamins (rod-domain in dark grey and Ig-domain in red), NPCs (blue) and the INM and ONM (transparent grey), were modeled into a region of a cryo-tomogram containing the lamin meshwork (see Fig. 1a). (b) Comparison between cytoskeletal elements in 4 nm thick tomogram slices shows MTs, actin, vimentin and the lamins with their respective diameters. Scale bar, 20 nm.